Imaging rapid early afterslip of the 2016 Pedernales earthquake, Ecuador

Louisa L.H. Tsang, Mathilde Vergnolle, Cedric Twardzik, Anthony Sladen, Jean-Mathieu Nocquet, Frédérique Rolandone, Hans Agurto-Detzel, Olivier Cavalié, Paul Jarrin, Patricia Mothes

Imaging rapid early afterslip of the 2016 Pedernales earthquake, Ecuador

Louisa L.H. Tsang[1], Mathilde Vergnolle[1], Cedric Twardzik[1], Anthony Sladen[1], Jean-Mathieu Nocquet[1,2], Frédérique Rolandone[3], Hans Agurto-Detzel[1], Olivier Cavalié[1,4], Paul Jarrin[1,3], Patricia Mothes[5]

1. Université Côte d'Azur, CNRS, Observatoire de la Côte d'Azur, IRD, Géoazur, Campus CNRS, 250 rue Albert Einstein, Sophia Antipolis 06560 Valbonne, France.

2. Université de Paris, UMR 7154 CNRS, Paris, France.

3. Sorbonne Université, CNRS-INSU, Institut des Sciences de la Terre Paris, ISTeP UMR 7193, F-75005, Paris, France.

4. Université de Lyon, UCBL, CNRS, LBL-TPE, 69622 Villeurbanne, France.

5. Instituto Geofísico, Escuela Politécnica Nacional, 2759 Quito, Ecuador.

Corresponding author:

Louisa L.H. Tsang. louisa.tsang@geoazur.unice.fr

Present address:

Géoazur, Campus CNRS, 250 rue Albert Einstein, Sophia Antipolis 06560 Valbonne, France.

Abstract

High-Rate (HR) GPS time series following the 2016 M_w 7.8 Pedernales earthquake suggest significant postseismic deformation occurring in the early postseismic period (i.e. first few hours after the earthquake) that is not captured in daily GPS time series. To understand the characteristics of early postseismic deformation, and its relationship with the mainshock rupture area, aftershocks and longer-term postseismic deformation, we estimate the spatio-temporal distribution of early afterslip with HR-GPS time series that span ~ 2.5 minutes to 72 hours after the earthquake, and compare with afterslip models estimated with daily GPS time series spanning a similar postseismic time period and up to 30 days after the earthquake. Our inversion technique enables us to image the nucleation of afterslip in the initial hours after the earthquake, bringing us closer to the transition between the coseismic and postseismic phases. The spatial signature of early afterslip in the region updip of the mainshock rupture area is consistent with longer-term afterslip that occurs in the 30-day postseismic period, indicating that afterslip nucleated updip of and adjacent to peak coseismic slip asperities, in two localized areas, and subsequently continued to grow in amplitude with time in these specific areas. A striking difference, however, is that inversion of the 72-hour HR-GPS time series suggests early afterslip within the mainshock rupture area, but which may have been short-lived. More interestingly, we find that postseismic slip starts immediately after the earthquake at a rapid rate. Indeed, we find that early afterslip represents a significant contribution to the postseismic geodetic moment – afterslip in the first 72 hours is ~60 % greater than that estimated with daily GPS time series that span the first three post-earthquake daily GPS positions (i.e. covering the same time window). The results of our study demonstrate that imaging the spatio-temporal evolution of afterslip using subdaily GPS time series is important for evaluating postseismic slip

budgets, and provides additional insights into the postseismic slip behaviour of faults.

Keywords: afterslip; postseismic; subduction; Ecuador; aftershocks; GPS

1. Introduction

Afterslip plays an important role in redistributing stresses on and around megathrusts following subduction zone earthquakes, and can represent a significant amount of moment release [e.g. Hsu et al., 2006]. Thus, mapping out at various timescales where it occurs is vital for assessing seismic hazard on neighbouring sections of megathrusts. Most afterslip imaging studies are conducted using daily GPS time series spanning timescales ranging from weeks to years following the earthquake [e.g. Hsu et al., 2006; Tsang et al., 2016]. The first data point in these postseismic time series is at best taken on the first, or the second day, after the earthquake. However, these postseismic daily GPS time series do not enable us to understand the nature of postseismic deformation occurring in the minutes to hours following the earthquake, hereafter referred to as the early postseismic period. Rather, early postseismic deformation is commonly captured within the static coseismic offset calculated with InSAR or daily GPS time series spanning a certain number of days before and after the earthquake. This manner of calculation can result in a contamination of the coseismic signal by early postseismic deformation, resulting in potential biases in the estimated coseismic source model. This likely explains why seismic moments for the same earthquake estimated from only daily GPS measurements can range from 1.5 to 2 times higher than those using only seismic data [e.g. Langbein et al., 2006]. Furthermore, daily GPS time series do not allow us to resolve the transition between the coseismic and postseismic phases of deformation, and can hence potentially result in erroneous estimates of coseismic and postseismic slip budgets on faults. Thus, better understanding the early phase of postseismic deformation requires analysis of high-rate GNSS position time series that can capture the associated signal on the Earth's surface.

Thus far, only a handful of studies have focused on the early postseismic period. These studies focus on the 2004 M_w 6.0 Parkfield earthquake in California [Langbein et al., 2006], 2003 M_w 8.0 Tokachi-Oki [Miyazaki and Larson, 2008; Fukuda et al., 2009] and 2011 M_w 9.1 Tohoku-oki earthquakes [Munekane, 2013] in Japan, 2012 M_w 7.6 Nicoya earthquake in Costa Rica [Malservisi et al., 2012], and the 2010 M_w 8.8 Maule, 2014 M_w 8.3 Illapel and 2016 M_w 7.8 Pedernales earthquakes in South America [Twardzik et al., 2019]. By analyzing HR-GPS position time series following these earthquakes, these studies demonstrate that the magnitude of early postseismic deformation is significant. For example, the geodetic moment in the early postseismic period following the 2012 Nicoya earthquake represents ~57 % of that released during the first 70 days [Malservisi et al., 2012]. Malservisi et al. [2012] and Munekane [2013] estimated snapshots of the spatial distribution of early afterslip by inverting cumulative offsets calculated with a certain length time window of HR-GPS time series. However, this approach does not enable us to ensure coherency of afterslip from one time step to another. Also, it should be noted that cumulative offsets calculated with HR-GPS time series can vary depending on the level of noise in the time series and the method used to calculate these offsets. Of the studies mentioned above, only Miyazaki and Larson [2008] inverted HR-GPS time series (spanning 4 hours after 2003 Tokachi-oki earthquake) to image the spatio-temporal evolution of afterslip. Their results show a complex evolution of early afterslip and suggest that it might have triggered the aftershock that occurred ~1.2 hours after the mainshock. They concluded that depth-dependent properties on the fault influence the propagation patterns of afterslip seen in their models. Fukuda et al. [2009] investigated postseismic time series of this earthquake too, with a focus on the sudden acceleration of motions ~1.2 hours after the earthquake. They argue that the timing of this acceleration phase is driven by stress changes from the mainshock

and the frictional parameters of the rate-and-state friction law, rather than due to the timing of the aftershock. Their results support theoretical studies demonstrating that faults experience an initial acceleration phase of afterslip, which is then followed by decelerating afterslip governed by steady-state velocity-strengthening friction [Perfettini and Ampuero, 2008]. Clearly, investigating the spatio-temporal evolution of early postseismic deformation is relevant for understanding the physical mechanisms driving fault slip behaviour, as well as resolving its relationship with the mainshock rupture area, ensuing aftershocks, longer-term postseismic deformation, and quantifying its contribution to the postseismic slip budget.

Here, we model HR-GPS postseismic time series to estimate the spatio-temporal evolution of early afterslip following the 2016 M_w 7.8 Pedernales earthquake (16 April 2016, 23:58:33) in Ecuador (Figure 1). The Ecuadorian megathrust hosts a diverse range of seismic and aseismic behaviour that has been studied in detail with regional GPS and seismic networks, as well as marine seismic studies [e.g., Collot et al., 2017; Font et al., 2013; Vallée et al., 2013; Mothes et al., 2013; Chlieh et al., 2014; Nocquet et al., 2014; 2016; Marcaillou et al., 2016; Rolandone et al., 2018; Gombert et al., 2018; Vaca et al., 2018; Segovia et al., 2018; Agurto-Detzel et al. (submitted); Twardzik et al., 2019]. The optimal location of these networks have enabled detection of a number of slow slip events, repeating earthquakes and seismic swarms, as well as significant afterslip in the month following the Pedernales earthquake [Vallée et al., 2013; Rolandone et al., 2018; Vaca et al., 2018; Segovia et al., 2018]. These findings indicate that aseismic slip processes represent a significant mode of strain release along the megathrust, and it is therefore important to understand their contribution to megathrust slip budgets.

In this study, we capitalize on the availability of rich postseismic geodetic datasets from Twardzik et al. [2019] and Rolandone et al. [2018] to image the spatio-temporal distribution of early afterslip in the first 72 hours after the earthquake, and compare this to afterslip estimated with daily GPS time series spanning the same time period (i.e. the first three post-earthquake daily GPS positions), as well as spanning the longer, 30-day post-earthquake time period (Figure 2). We also examine relationships between early afterslip, the earthquake rupture area, and the spatio-temporal distribution of relocated aftershocks.

2. Data

We use GPS data from 27 stations of the Ecuadorian continuous GPS network that were installed before the earthquake, and from which both HR-GPS and daily GPS time series were available (Figure 3). The horizontal components of the daily GPS time series from these stations were processed by Rolandone et al. [2018], with positions expressed with respect to the first daily GPS position (the day after the earthquake). In the days following the earthquake, 4 $M_w > 6$ aftershocks occurred in the region updip of the mainshock rupture area. Coseismic offsets (and likely some ensuing postseismic deformation) associated with these aftershocks are visible in the time series of stations CABP and MOMP on the 22 and 20 April, respectively (Figure S1). We did not attempt to correct the time series for these offsets, due to the absence of a technique to reliably estimate and remove the coseismic and postseismic signals associated with these aftershocks. No visible offsets associated with these aftershocks are observed at other stations.

The 30-second HR-GPS time series from these stations were processed by Twardzik et al. [2019]. The time series span ~72 hours after the earthquake from 17 April 2016, 00:02:00 to 19 April 2016, 23:59:59. The first position in the HR-GPS time series was chosen to ensure that the time series are not contaminated by seismic waves associated with the mainshock (see Twardzik et al. [2019] for details). We downsampled these time series to a position every 60 seconds, and used only the horizontal component of displacements, as the vertical component of displacements have relatively low signal-to-noise ratios and large uncertainties.

142 We examined the gCMT catalog of regional earthquakes, and found no significant signals of
143 these earthquakes in the HR-GPS time series. The largest 72-hour cumulative displacements are
144 observed at stations nearest the mainshock rupture area (Figure 3): MOMP, CABP and PDNS,
145 with values of 5.5, 4.6 and 3.3 cm, respectively. The 30-day cumulative displacements for these
146 stations, calculated from the daily GPS time series, are 12.6, 11 and 7.2 cm, respectively.
147
148 The 60-second HR-GPS time series are relatively noisy (Figures S2, S3). Hence, to verify that
149 our inversion results are not significantly influenced by noise in the time series, we performed
150 four additional inversions with time series low-pass filtered at various cut-off frequencies, to
151 extract the reliable features of the models (Text S1, Figure S3) (see next section for details).

3. Inversion method to estimate the spatio-temporal distribution of afterslip

We assume that the signal in the early postseismic time series represents predominantly afterslip on the megathrust. This approximation seems valid considering that postseismic signals are recorded at stations covering a region greater than would be expected from poroelastic effects, the latter of which are likely to occur in more localized regions [e.g. Tung and Masterlark, 2018]. Also, the early postseismic time period considered is shorter than characteristic relaxation times associated with typical mantle viscosities previously reported at subduction zones (assuming a linear mantle rheology, mantle viscosities of 10^{17} to $5*10^{19}$ Pa s correspond to relaxation times ranging from ~38 days to 50 years). Even so, we do not exclude the possibility that our modelling approach might represent deformation associated with other postseismic mechanisms mapped onto the fault. We estimated the spatio-temporal distribution of afterslip that span the first: (1) 72 hours (with HR-GPS time series), (2) 2 days (with time series of the first three daily GPS positions), and (3) 30 days (with daily GPS time series) (Figure 2). While Rolandone et al. [2018] already published a spatio-temporal 30-day afterslip model, we estimated the spatio-temporal 2-day and 30-day models using the same inversion strategy as that used to estimate the 72-hour model, in order to enable a fair comparison between them.

Since the HR-GPS time series are relatively noisy compared to daily GPS time series, a method is required to filter for the main postseismic signal in the presence of considerable noise in the time series. We adopted the Principal Component Analysis-based Inversion Method (PCAIM) [Kositsky and Avouac, 2010] to invert for the spatio-temporal distribution of afterslip, as this method allows the main postseismic signal to be represented with a small number of principal components. The surface displacement patterns associated with each principal component are

inverted to obtain a principal slip distribution; these are then linearly combined together with the corresponding time functions to obtain a model of the spatio-temporal evolution of afterslip (Text S2). While PCAIM has been validated on standard daily GPS time series, to the best of our knowledge it has never been implemented yet with noisy HR-GPS time series. However, it has been shown to be effective in estimating afterslip with noisy daily GPS time series [e.g. Gualandi et al., 2014]. To determine the optimum number of principal components to represent the postseismic signal, we analysed the time series fits as incrementally more principal components were employed, examined the time functions, surface displacement patterns associated with each principal component, and the corresponding principal slip patterns.

For the HR-GPS time series, we found that one principal component adequately represents the postseismic signal (Text S2, Figure S4), while for the daily GPS time series, two principal components were required (Figure S5). The additional component for the latter case is probably due to the presence of a slow slip event in the daily GPS time series (discussed in section 5.6). Offsets in the daily GPS time series seen at stations CABP and MOMP mentioned previously are not present in the time functions of the first two principal components, when the data are decomposed. Therefore, inclusion of these offsets does not significantly influence the afterslip model results.

We estimated afterslip on the same fault interface geometry employed by Rolandone et al. [2018]. This fault geometry spans latitudes ~2°S to ~1°N, extends to a depth of 80 km, and follows the SLAB1.0 model along this section of the Andean megathrust [Hayes et al., 2012].

198 The fault interface was discretized into quasi-equilateral triangles with 10-km-long edges. The
199 horizontal displacements at each GPS station due to slip on each sub-fault patch were calculated
200 with Okada's solutions for deformation due to point dislocations embedded in a homogeneous
201 elastic half-space [Okada, 1992]. Similar to the approach of Rolandone et al. [2018], the rake
202 angle on each triangular patch was fixed to a direction that is consistent with the Nazca/North
203 Andean block relative velocity determined by Nocquet et al. [2014] (although we note that
204 allowing the rake angle to vary by +/- 45° from 90° does not significantly affect the results;
205 Figure S6). Positivity constraints were applied to ensure trench-directed slip.
206
207 The Laplacian constraints, which control the degree that slip is smoothed across neighbouring
208 patches, were weighted spatially based on the sensitivity of each station to slip on each sub-fault
209 patch (following the method of Ortega-Culaciati [2013]). The spatial variation of this weighting
210 results in more smoothing of slip in poorly resolved areas (Text S3, Figure S7). In addition, λ,
211 the value controlling the strength of the Laplacian constraints, was selected for each model
212 based on the standard L-curve analysis [Hansen, 1992], corroborated by visual examination of
213 the slip distributions associated with each value of λ. The optimum value of λ represents the
214 best trade-off between the data-model misfits and the model norm, and which preserves the
215 key spatial characteristics of the solution (Text S3, Figure S8). We note that the optimum value
216 of λ differs by three orders of magnitude between the case of inverting the HR-GPS and the
217 daily GPS time series, because in the case of the daily GPS time series, we took into account
218 the data uncertainties (although we retrieve a similar spatial distribution of slip even if we do
219 not take into account the data uncertainties). On the other hand, we did not take into account
220 the uncertainties of the HR-GPS data in the inversion, as these could not be reliably estimated.

As mentioned in the previous section, for the 72-hour dataset, we performed five inversions, with each inversion using time series with various degrees of filtering applied, in order to extract the reliable features of afterslip. Our reference model is the afterslip distribution estimated with time series filtered with a cut-off frequency corresponding to a time period of ~2.7 hours, chosen as it yields visually smooth time series (Text S1).

4. Results

4.1. Early afterslip distribution from the 72-hour dataset

Six main early afterslip areas are evident in all five models (Areas A-F, Figure 3, inset, and Figure S9). The five models indicate geodetic moments ranging from 5.16E+19 to 6.35E+19 N m (M_w 7.11-7.17), assuming a rigidity of 30 GPa (Table S1).

Our reference model, shown in Figure 3, yields a reduced chi-square of 0.65. Assuming a rigidity of 30 GPa, the estimated total geodetic moment is 5.22E+19 N m, which is equivalent to a moment magnitude of M_w 7.11. This moment estimate is ~9.7% of the coseismic moment as estimated by Nocquet et al. [2016]. The model shows peak cumulative afterslip of ~ 30 cm concentrated in two areas updip of and adjacent to asperities that experienced the largest coseismic slip (Areas A and B). The largest cumulative geodetic moment occurred in area A (9.25E+18 N m; M_w 6.61), while less occurred in area B (8.28E+18 N m; M_w 6.58). In addition, ~13-18 cm of cumulative afterslip is concentrated within the southern portion of the mainshock rupture area (area C) and immediately downdip of the mainshock rupture area (area D), with each area amounting to an estimated geodetic moment of 1.02E+19 N m (M_w 6.63). ~1.67E+18 N m (M_w 6.12) of geodetic moment is estimated north of the mainshock rupture area (area E).

Further south-east, ~190 km from the Pedernales earthquake hypocentre, ~ 28 cm of cumulative slip is estimated on a single patch located north of La Plata Island (area F, Figure 3). This patch of slip is located close to the remotely triggered slow slip event that was reported by Rolandone et al. [2018]; we discuss these results in section 5.6.

While we demonstrate that the main afterslip areas shown in Figure 3 (inset) are reliable based on inverting various groups of filtered time series, we additionally conducted synthetic tests (in the next section) to assess the resolution of slip in our reference model, which is related to the fault geometry that we employed and the spatial distribution of GPS stations.

4.2. **Model resolution**

For each main afterslip area, 1 m of trench-perpendicular slip was assigned to each sub-fault patch. Then, horizontal displacements at each station were calculated with the Okada model [Okada, 1992]. Synthetic time series at each station were subsequently calculated by multiplying the horizontal displacements with the synthetic normalized time function (based on the first principal component obtained from decomposition of the 30-day GPS time series). For each station, noise was added to the synthetic time series that is on the order of the average standard deviation from the mean position estimated using the pre-earthquake HR-GPS time series (Figure S2). For the inversion, we employed the same value of λ as that in our reference model.

The magnitude of peak slip is well recovered in the two areas updip of the mainshock rupture area (Figure 4a), as well as within the mainshock rupture area (Figure 4b), as the inversion indicates that ~ 73-78 % of the input synthetic slip is recovered. On the other hand, the magnitude of peak slip is not well recovered downdip of the mainshock rupture area (Figure 4c), and near Esmeraldas (Figure 4d), with only ~ 30-38 % of the input synthetic slip recovered in the inversion, and significant smoothing of slip across adjacent sub-fault patches. These conclusions are supported by the recovered slip model based on an input model where all main afterslip areas were assigned trench-perpendicular synthetic slip of 1 m (Figure 4e); slip in the updip regions is well recovered, while slip downdip and near Esmeraldas is not. In the mainshock rupture area, slip is recovered, but is smeared across neighbouring sub-fault patches. Importantly, Figure 4a demonstrates that slip in the southern updip area is not smeared into the mainshock rupture area, suggesting that slip in area C (Figure 3) is not an artifact of the spatial

277 smoothing that we employ. In addition, slip in area C is evident in rougher afterslip models from
278 all five inversions (Figure S8), suggesting that this is a reliable feature, since it is evident
279 regardless of the temporal smoothing of the time series and spatial smoothing of slip.
280
281 We present in Text S4 and Figure S11 results of implementing an alternative method of
282 assessing the resolution of our model. The results substantiate our conclusions drawn here.
283 Furthermore, Rolandone et al. [2018] reported that slip areas of > 40 km on this fault
284 geometry are well resolved.

285 ## 5. Discussion

286 ### 5.1. Comparison of 72-hour and 2-day afterslip models highlights the
287 significant contribution of early afterslip

288 Figure 5 and Table 1 show that in each of the six main afterslip areas, the geodetic moment of
289 afterslip in the 72-hour model is greater than that in the 2-day model. The 72-hour model
290 suggests afterslip in two areas that are not visually evident in the 2-day model: north of the
291 mainshock rupture area near Esmeraldas and north of La Plata Island (areas E and F,
292 respectively, Figure 5c), where the difference in geodetic moment is a factor of ~43 and 2.6,
293 respectively. However, our model resolution tests suggest that slip is not well resolved in these
294 two areas. In other areas (areas A-D), the geodetic moment between the two models differs by
295 a factor of ~1.5 to 2.3. These findings suggest enhanced afterslip in these areas during the first
296 12 hours, the period that is not captured by the daily GPS time series.
297
298 South of the mainshock rupture area (area G, Figure 5c), more afterslip is estimated in the 2-
299 day model. According to our approach of extracting the robust features of the 72-hour model
300 based on various filtered time series (Figure S9), slip here is not a reliable feature and may be
301 due to high frequency noise in the time series. Slip here in the 72-hour model is thus not
302 accurately resolved.
303
304 Overall, the estimated geodetic moment of the 72-hour model is a factor of ~1.6 greater than
305 that of the 2-day model (Table 1) (this factor is ~1.68 in the case of excluding poorly resolved
306 slip areas), suggesting that not accounting for the postseismic deformation recorded
307 immediately after the coseismic phase could result in an underestimation of the postseismic

308 geodetic moment by ~60 % - very early afterslip (i.e. before the first GPS daily position)
309 therefore contributes significantly to the postseismic geodetic moment.
310
311 Our 72-hour afterslip model explains why coseismic slip distributions estimated with InSAR
312 data place coseismic slip near the trench. For example, from InSAR data that span 6 days after
313 the earthquake, He et al. [2017] found coseismic slip that extends to regions near the trench,
314 and a higher estimated seismic moment compared with studies that either exclude or put a low
315 weighting on InSAR data [e.g. Nocquet et al., 2016; Ye et al., 2016]. As the InSAR data likely
316 contain deformation due to both the coseismic and early postseismic slip, their models are
317 consistent with our results showing early afterslip located updip of the mainshock rupture area.

5.2. Spatio-temporal evolution of afterslip and aftershocks in the first 72 hours

Figure 6 shows how afterslip evolves in time within the 72-hour period. As pointed out by Rolandone et al. [2018], the spatial distribution of shallow afterslip shows little correspondence to that of stress changes induced by coseismic slip. Interestingly, our results suggest that this spatial distribution, where slip is localized in a few specific areas rather than broadly updip and downdip of the rupture area, is in place immediately after the earthquake. In the subsequent 72-hour postseismic period, the spatial distribution of afterslip remains fixed, with the amplitude of afterslip increasing with time. This latter finding is expected given that only one principal component was used (and is sufficient) to represent the postseismic time series, such that the slip evolution on each patch is governed by the same time function. This specificity of using one principal component also limits our capability to discern possible patterns of accelerating afterslip in the different afterslip areas. Importantly, our spatio-temporal modelling approach enables us to analyze an enriched picture of the temporal evolution of afterslip that indicates that the highlighted updip areas are particularly prone to host afterslip, and enables us to compare our results with the spatio-temporal evolution of aftershocks.

Aftershocks occur due to the release of static and/or dynamic stress changes associated with the mainshock [Dieterich, 1994; Felzer and Brodsky, 2006; Stein, 1999]. In addition, a number of studies have reported similar temporal evolution of afterslip and aftershocks following large earthquakes, which support a model whereby aftershocks are produced when rate-weakening asperities are loaded by afterslip and driven to coseismic failure [e.g. Hsu et al., 2006; Perfettini and Avouac, 2004]. To explore the spatio-temporal relationship between afterslip and aftershocks in the first 72 hours, we analyzed the aftershock catalogue of Agurto-Detzel et al.

(submitted). Errors in the aftershock locations at the 68 % confidence level are ~12 and 13 km in the horizontal and vertical directions, respectively. Based on their one-year-long aftershock catalogue, Agurto-Detzel et al. (submitted) reported a threshold magnitude of completeness of 2.5. However, the catalogue is most likely incomplete in the initial hours after the earthquake, as during this period the noise level is higher and events are harder to identify. To be more conservative, we therefore analyzed $M_L \geq 3.5$ aftershocks in this study (Figure S12).

Figure 6 shows that relocated M3.5+ aftershocks appear to concentrate in regions bordering the two updip peak afterslip areas (A and B), which is consistent with the results from other studies that reported limited occurrence of aftershocks within the regions of peak afterslip [e.g. Hobbs et al., 2017; Hsu et al., 2006]. In area A, the aftershock-afterslip moment ratio, expressed as a percentage of the cumulative aftershock seismic moment to the cumulative afterslip geodetic moment, is 11%, while in area B, this ratio is ~ 6% (seismicity in each area is defined using the limits shown in Figure S12). These ratios indicate that the majority of the postseismic deformation is aseismic. A large number of aftershocks are also located within the mainshock rupture area; these occur in the region between the two peak coseismic slip asperities, and border the patches of peak afterslip in area C. However, the cumulative seismic moment released in area C is small - the aftershock-afterslip moment ratio is 0.93 %; around an order of magnitude smaller than in the two updip afterslip regions. In contrast, there is sparse seismicity in the region downdip of the mainshock.

In the first 72 hours, the similarity in the temporal evolution of afterslip and numbers of $M_L >$ 3.5 aftershocks in the two updip areas (A and B) (Figure 7) suggests that aftershocks in these

364 regions are likely driven by afterslip, consistent with the findings of Agurto-Detzel et al.
365 (submitted) based on their one-year-long catalogue. In contrast, the evolution curves suggest
366 that in area C, there is a much larger fraction of aftershock occurrence in the first ~48 hours
367 compared to other areas (Figure 7). We hypothesize that a proportion of aftershocks
368 represent the release of residual coseismically-induced stress on the megathrust interface as
369 well as in the overlying crust (Figure S12), and are thus possibly controlled by two different
370 processes. In addition, though our analysis may be limited by the completeness of the
371 aftershock catalogue in the first 72 hours, the evolution curves (note that Figure 7 is in semi-
372 logarithmic scale) suggest that early afterslip and aftershocks do not appear to follow an Omori-
373 type law, in contrast to findings from analyzing aftershocks over a longer time period of ~1 year
374 [Agurto-Detzel et al. (submitted)].
375
376 Interestingly, the 1942 earthquake has been inferred to have roughly the same rupture area as
377 the 2016 earthquake [Ye et al., 2016; Nocquet et al., 2016], and aftershocks following the 1942
378 earthquake were mainly located seaward of the hypocentre [Mendoza and Dewey, 1984],
379 implying that these aftershocks may have been driven by afterslip updip of the mainshock
380 rupture area too. If so, these observations may indicate that aseismic slip behaviour, and by
381 inference, frictional properties, persist through at least two seismic cycles.

5.3. 30-day afterslip distribution from daily GPS time series

Our 30-day afterslip results (Figure 8b) are consistent with that estimated by Rolandone et al. [2018] (data-model fits at representative stations are shown in Figure 8d; the spatio-temporal evolution of afterslip in the first 30 days and data-model time series fits at all stations are shown in Figures S13 and S14, respectively). Estimated afterslip in the first 30 days amounts to a geodetic moment of 1.71E+20 N m, equivalent to an ~M_w 7.46. In the region updip of the mainshock rupture area, the spatial distribution of 30-day afterslip is consistent with that in the first 72 hours, indicating that afterslip nucleated in localized areas updip of and adjacent to patches that experienced the largest coseismic slip, and subsequently continued to grow in amplitude with time. Similar to the case within the first 72 hours, aftershocks in the subsequent 28 days mostly surround the updip afterslip areas (Figure 8b). Peak afterslip is concentrated in area B (~70 cm) and might have extended to the trench, though the model resolution is poor close to the trench. In both areas A and B, estimated afterslip in the first 72 hours is ~30 % of that accumulated in the first 30 days (Table 1).

On the other hand, there are differences between the 72-hour and 30-day afterslip models within, downdip and north of the mainshock rupture area (areas C, D and E, respectively). In area E, we have already pointed out that resolution of slip here in the 72-hour model is poor (see section 4.2). In area C, where slip is better resolved, a greater amount of afterslip likely occurred in the first 72 hours, but this afterslip may have been short-lived, as limited afterslip is imaged in these areas in the 30-day model. Also, notwithstanding the poorer model resolution in the downdip region, a comparison of the two models shows that afterslip here nucleated in

404 the first 72 hours immediately downdip of the mainshock rupture at ~ 30-50 km depths, and

405 may have subsequently migrated southwards and extended to ~40-70 km depths.

406 **5.4. Spatial overlap of early afterslip with the mainshock rupture area**

407 Comparison of our 72-hour, 2-day and 30-day models suggests that afterslip in the mainshock
408 rupture zone rapidly decayed with time, likely within the first 12 hours after the earthquake.
409 There is a spectrum of observations concerning afterslip occurring in mainshock rupture zones.
410 Some studies have reported observations of coseismic deformation that is anticorrelated with
411 afterslip and/or aftershock areas [e.g. Perfettini et al., 2010; Sladen et al., 2010]. These studies
412 support the 'rate-state asperity model' that stipulates that velocity-weakening patches on the
413 fault that host seismic ruptures do not manifest significant afterslip. On the other hand, a
414 number of recent studies report that afterslip in coseismic rupture zones is needed to explain
415 geodetic observations, challenging this conceptual model [e.g. Barnhart et al., 2016; Bedford et
416 al., 2013; Miyazaki and Larson, 2008; Johnson et al., 2012; Salman et al., 2017]. It is possible that
417 some of these observations can be explained by modelling biases. For example, coseismic slip
418 distributions estimated with InSAR data often span the early and longer postseismic period,
419 which potentially results in some amount of postseismic deformation being mapped as
420 coseismic slip. Another bias may lie in the choice of model smoothing parameters for
421 postseismic slip models [e.g. Fukuda et al., 2009].
422
423 Despite these biases, several physical mechanisms have been proposed to explain the overlap of
424 afterslip and coseismic slip areas. Helmstetter and Shaw [2009] stipulate that frictional
425 properties on the megathrust are not steady state. Physical processes such as dynamic
426 weakening and rupture directivity may push normally velocity-strengthening patches to
427 participate in coseismic ruptures [e.g. Noda and Lapusta, 2013, Salman et al. 2017]. Along the
428 Ecuadorian subduction zone, Kanamori and McNally [1982] proposed a model in which distinct

429 'asperities' of the 1942, 1958 and 1979 ruptures are separated by weak zones that typically
430 behave aseismically, but can slip abruptly when driven by failure of neighbouring asperities - this
431 mechanism was proposed to explain the coordinated rupture of all three asperities in a M_w 8.8
432 earthquake in 1906. Indeed, frictional properties may vary during the course of the earthquake
433 cycle, and patches that are conditionally stable may participate in both coseismic and aseismic
434 slip phases. Yabe and Ide [2018] modeled a frictionally heterogeneous fault system and their
435 quasi-dynamic numerical simulation results were able to reproduce afterslip and aftershocks
436 occurring around and within the mainshock rupture zone. They proposed that if patches within
437 the mainshock rupture zone do not fully release the accumulated slip deficit, afterslip and
438 aftershocks on these patches are a plausible mechanism through which the residual slip deficit
439 can be released. In addition, Agurto-Detzel et al. (submitted) proposed that mainshock-
440 reactivated processes in the damage zone above the mainshock rupture area might explain the
441 large density of aftershocks located on and above the megathrust interface, in the first ~24
442 hours. From these perspectives, we hypothesize that the occurrence of rapidly decaying early
443 afterslip in the mainshock rupture area could be explained by: (1) time-variable conditions that
444 can alter the stress state, stability or frictional properties of patches, enabling patches in the
445 mainshock rupture area to host afterslip, (2) release of the residual slip deficit during the short
446 time frame after the mainshock, and/or (3) deformation within the volume surrounding the
447 megathrust interface due to stress changes induced by the mainshock.

448 **5.5. Spatial distribution of afterslip controlled by features on the incoming plate**

449 The southern limit of updip afterslip (area A) overlaps with a highly coupled region (Figure 8c),
450 and is marked by a high density of interseismic (see Font et al. [2013]) as well as aftershock
451 seismicity (Figure 8b). The location of this seismicity cluster coincides with the northern flank of
452 the Carnegie Ridge. Flanks of ridges have been proposed to be rough [Bassett and Watts,
453 2015]; seismicity here may hence reflect the roughness of the subducting plate [Agurto-Detzel
454 et al. (submitted)]. Also, south of this area, interseismic slip deficit maps indicate a 'creeping
455 corridor', which may be related to the strike-slip Jama Fault Zone that extends down to the
456 megathrust interface [Chlieh et al., 2014], and that may have influenced the southern extent of
457 afterslip.

458

459 In the north, a distinct cluster of aftershocks aligns with the northern extent of afterslip in area
460 B (Figures 8b). The northern extent of afterslip in area B appears to be mostly confined to the
461 region south of this cluster of aftershocks. North of this cluster lies the zone that ruptured
462 during the 1958 earthquake, and where the interseismic slip deficit is higher in regions close to
463 the trench (Figure 8c).

464

465 Strikingly, less afterslip occurs in the updip region between areas A and B, where a double
466 peaked seamount and associated pervasive fracturing was imaged by Marcaillou et al. [2016]
467 (Figure 8). We hypothesize that properties around the subducting seamount may inhibit the
468 pervasive propagation of afterslip into this region. Collectively, these observations suggest that
469 features on the incoming plate exert a strong control on the along-strike segmentation of

afterslip along this section of the Ecuadorian megathrust, in agreement with the hypothesis proposed by Agurto-Detzel et al. (submitted).

5.6. A slow slip event near La Plata Island

Daily time series at GPS stations located near La Plata Island (ISPT, MHLA, SLGO) are indicative of a slow slip event (SSE) in this region, with typical phases of increasing velocities then decreasing velocities of deformation (Figure 8d). This SSE was possibly remotely triggered by static stress changes caused by the mainshock rupture [Rolandone et al., 2018]. Our inversion results suggest that this SSE occurred trenchward of the section of the megathrust under La Plata Island (area F, Figure 8b), consistent with the results of Rolandone et al. [2018]. The estimated geodetic moment of the SSE is 1.03E+19 (~M_w 6.6). Intriguingly, our 72-hour model shows slip on a single patch north of La Plata Island amounting to a geodetic moment of 8.86E+17 N m (M_w 5.93) (Figure 8a) that may suggest onset of the SSE in the early postseismic period, although this patch is poorly resolved. Coincidentally, seismicity is also concentrated in the region north of La Plata Island in the first three days, before then occurring in regions south and trenchwards of the island (Figure S13). If we suppose that this seismicity reflects an underlying SSE driving mechanism, we speculate that the SSE might have nucleated north of La Plata Island and migrated southwards and trenchwards with time. However, our speculation should be substantiated with studies of longer HR-GPS time series to better image its onset and migration.

6. Conclusions

We estimate the spatial and temporal distribution of afterslip spanning various timescales, ranging from ~ 2.5 minutes to 30 days after the earthquake, using HR-GPS and daily GPS time series. Although the HR-GPS time series are relatively noisy compared to the daily GPS time series, our employed inversion method enables us to invert the 72-hour HR-GPS time series to obtain a detailed description of the spatio-temporal evolution of early afterslip, and explore its spatial relation to longer-term afterslip, the mainshock rupture area, and ensuing aftershocks.

We find that the spatial signature of early afterslip in the first 72 hours within the region updip of the mainshock rupture area is consistent with that in the 30-day postseismic period, indicating that afterslip nucleated primarily updip of and adjacent to two peak coseismic slip asperities, and subsequently continued to grow in amplitude with time. The spatial pattern of afterslip appears to be localized in areas prone to host aseismic slip over several seismic cycles and controlled by features on the incoming plate. Interestingly, our results suggest that early afterslip may have occurred within part of the mainshock rupture area, but which may have decayed rapidly, as little afterslip is imaged here in the 30-day afterslip model.

One of our most important findings is that early afterslip (in the first 72 hours) following the Pedernales earthquake represents a significant contribution, ~30 %, to the postseismic geodetic moment over the first 30 days. Furthermore, not accounting for afterslip before the first daily GPS position (in this case, in the 12 hours after the earthquake) strongly biases the postseismic geodetic moment, with ~60% of postseismic geodetic moment missing over the first 72 hours.

511 We advocate the importance of imaging afterslip in the minutes to hours following earthquakes,
512 in order to better understand its contribution towards postseismic slip budgets on faults.
513

514 ## 7. Acknowledgements

515 We thank Hugo Perfettini for insightful, fruitful discussions and advice with implementing
516 PCAIM. We thank Francisco Ortega-Culaciati and Steven Tsang for insightful discussions.
517 Figures were produced with Generic Mapping Tools (GMT) [Wessel and Smith, 1998]. The
518 acquisition of the data was carried out by IG-EPN and IRD in the frame of the Joint
519 International Laboratory 'Seismes & Volcans dans les Andes du Nord'. We thank all the field
520 operators who participated in the acquisition of this data. This research was supported by the
521 Agence Nationale de la Recherche (ANR) project E-POST (M. Vergnolle, contract number
522 ANR-14-CE03-0002-01JCJC 'E-POST'). L. Tsang's postdoctoral fellowship is funded by the ANR
523 JCJC E-POST, and P. Jarrin's doctoral fellowship is funded by Senescyt - IFTH – Ecuador.

8. References

Agurto-Detzel, H., et al. Agurto-Detzel, H., Y. Font, P. Charvis, M. Régnier, A. Rietbrock, D. Ambrois, M. Paulatto, A. Alvarado, S. Beck, M.J. Hernandez, S. Hernandez, M. Hoskins, S. León-Ríos, C. Lynner, A. Meltzer, E. D. Mercerat, F. Michaud, J.M. Nocquet, F. Rolandone, M. Ruiz and L. Soto-Cordero. Ridge subduction and afterslip control aftershock distribution of the 2016 M_w 7.8 Ecuador earthquake (submitted).

Barnhart, W. D., J. R. Murray, R. W. Briggs, F. Gomez, C. P. Miles, J. Svarc, S. Riquelme, and B. J. Stressler (2016), Coseismic slip and early afterslip of the 2015 Illapel, Chile, earthquake: Implications for frictional heterogeneity and coastal uplift, *Journal of Geophysical Research: Solid Earth*, *121*(8), 6172-6191. doi: 10.1002/2016JB013124.

Bassett, D., and A. B. Watts (2015), Gravity anomalies, crustal structure, and seismicity at subduction zones: 1. Seafloor roughness and subducting relief, *Geochemistry, Geophysics, Geosystems*, *16*(5), 1508-1540, doi:10.1002/2014GC005684.

Beck, S. L., and L. J. Ruff (1984), The rupture process of the Great 1979 Colombia Earthquake: Evidence for the asperity model, *Journal of Geophysical Research: Solid Earth*, *89*(B11), 9281-9291, doi:10.1029/JB089iB11p09281.

Bedford, J., et al. (2013), A high-resolution, time-variable afterslip model for the 2010 Maule M_w = 8.8, Chile megathrust earthquake, *Earth and Planetary Science Letters*, *383*, 26-36, doi:10.1016/j.epsl.2013.09.020.

543 Chlieh, M., et al. (2014), Distribution of discrete seismic asperities and aseismic slip along the
544 Ecuadorian megathrust, *Earth and Planetary Science Letters*, *400*, 292-301,
545 doi:10.1016/j.epsl.2014.05.027.

546 Collot, J.-Y., E. Sanclemente, J.-M. Nocquet, A. Leprêtre, A. Ribodetti, P. Jarrin, M. Chlieh, D.
547 Graindorge, and P. Charvis (2017), Subducted oceanic relief locks the shallow megathrust in
548 central Ecuador, *Journal of Geophysical Research: Solid Earth*, *122*(5), 3286-3305. doi:
549 10.1002/2016JB013849.

550 Dieterich, J. (1994), A constitutive law for rate of earthquake production and its application to
551 earthquake clustering, *Journal of Geophysical Research: Solid Earth*, *99*(B2), 2601-2618,
552 doi:doi:10.1029/93JB02581.

553 Felzer, K. R., and E. E. Brodsky (2006), Decay of aftershock density with distance indicates
554 triggering by dynamic stress, *Nature*, *441*, 735-738, doi:10.1038/nature04799.

555 Font, Y., M. Segovia, S. Vaca, and T. Theunissen (2013), Seismicity patterns along the Ecuadorian
556 subduction zone: new constraints from earthquake location in a 3-D a priori velocity model,
557 *Geophysical Journal International*, *193*(1), 263-286, doi:10.1093/gji/ggs083.

558 Fukuda, J. i., K. M. Johnson, K. M. Larson, and S. i. Miyazaki (2009), Fault friction parameters
559 inferred from the early stages of afterslip following the 2003 Tokachi-oki earthquake, *Journal of*
560 *Geophysical Research: Solid Earth*, *114*(B4), doi:10.1029/2008JB006166.

561 Gombert, B., Z. Duputel, R. Jolivet, M. Simons, J. Jiang, C. Liang, E. J. Fielding, and L. Rivera
562 (2018), Strain budget of the Ecuador–Colombia subduction zone: A stochastic view, *Earth and*
563 *Planetary Science Letters*, *498*, 288-299, doi:10.1016/j.epsl.2018.06.046.

564 Gualandi, A., E. Serpelloni, and M. Belardinelli (2014), Space–time evolution of crustal
565 deformation related to the M_w 6.3, 2009 L'Aquila earthquake (central Italy) from principal
566 component analysis inversion of GPS position time-series, *Geophysical Journal International*,
567 *197*(1), 174-191. doi: 10.1093/gji/ggt522.

568 Hansen, P. C. (1992), Analysis of discrete ill-posed problems by means of the L-curve, *SIAM*
569 *Rev.*, *34*(4), 561-580.

570 Hayes, G. P., D. J. Wald, and R. L. Johnson (2012), Slab1.0: A three-dimensional model of global
571 subduction zone geometries, *Journal of Geophysical Research: Solid Earth*, *117*(B1), B01302,
572 doi:10.1029/2011JB008524.

573 He, P., E. A. Hetland, Q. Wang, K. Ding, Y. Wen, and R. Zou (2017), Coseismic slip in the 2016
574 M_w 7.8 Ecuador earthquake imaged from Sentinel-1A radar interferometry, *Seismological*
575 *Research Letters*. doi: 10.1785/0220160151.

576 Helmstetter, A., and B. E. Shaw (2009), Afterslip and aftershocks in the rate-and-state friction
577 law, *Journal of Geophysical Research: Solid Earth*, *114*(B1). doi: 10.1029/2007JB005077.

578 Hobbs, T. E., C. Kyriakopoulos, A. V. Newman, M. Protti, and D. Yao (2017), Large and
579 primarily updip afterslip following the 2012 M_w 7.6 Nicoya, Costa Rica, earthquake, *Journal of*
580 *Geophysical Research: Solid Earth*, *122*(7), 5712-5728, doi:10.1002/2017JB014035.

581 Hsu, Y.-J., M. Simons, J.-P. Avouac, J. Galetzka, K. Sieh, M. Chlieh, D. Natawidjaja, L.
582 Prawirodirdjo, and Y. Bock (2006), Frictional Afterslip Following the 2005 Nias-Simeulue
583 Earthquake, Sumatra, *Science*, *312*(5782), 1921-1926, doi:10.1126/science.1126960.

584 Johnson, K. M., J. i. Fukuda, and P. Segall (2012), Challenging the rate-state asperity model:
585 Afterslip following the 2011 M9 Tohoku-oki, Japan, earthquake, *Geophysical Research Letters*,
586 *39*(20). doi: 10.1029/2012GL052901.

587 Kanamori, H., and K. C. McNally (1982), Variable rupture mode of the subduction zone along
588 the Ecuador-Colombia coast, *Bulletin of the Seismological Society of America*, *72*(4), 1241-1253.

589 Kositsky, A. P., and J. P. Avouac (2010), Inverting geodetic time series with a principal
590 component analysis-based inversion method, *Journal of Geophysical Research: Solid Earth*, *115*(B3),
591 B03401, doi:10.1029/2009JB006535.

592 Langbein, J. (2006), Coseismic and initial postseismic deformation from the 2004 Parkfield,
593 California, earthquake, observed by Global Positioning System, Electronic Distance Meter,
594 creepmeters, and borehole strainmeters, *Bulletin of the Seismological Society of America*, *96*(4B),
595 S304-S320, doi:10.1785/0120050823.

596 Malservisi, R., et al. (2015), Multiscale postseismic behavior on a megathrust: The 2012 Nicoya
597 earthquake, Costa Rica, *Geochemistry, Geophysics, Geosystems*, *16*(6), 1848-1864,
598 doi:10.1002/2015GC005794.

599 Marcaillou, B., J.-Y. Collot, A. Ribodetti, E. d'Acremont, A.-A. Mahamat, and A. Alvarado (2016),
600 Seamount subduction at the North-Ecuadorian convergent margin: Effects on structures, inter-
601 seismic coupling and seismogenesis, *Earth and Planetary Science Letters*, *433*, 146-158,
602 doi:10.1016/j.epsl.2015.10.043.

603 Mendoza, C., and J. W. Dewey (1984), Seismicity associated with the great Colombia-Ecuador
604 earthquakes of 1942, 1958, and 1979: Implications for barrier models of earthquake rupture,
605 *Bulletin of the Seismological Society of America*, *74*(2), 577-593.

606 Miyazaki, and K. M. Larson (2008), Coseismic and early postseismic slip for the 2003 Tokachi-
607 oki earthquake sequence inferred from GPS data, *Geophysical Research Letters*, *35*(4),
608 doi:10.1029/2007GL032309.

609 Mothes, P. A., J.-M. Nocquet, and P. Jarrín (2013), Continuous GPS network operating
610 throughout Ecuador, *Eos, Transactions American Geophysical Union*, *94*(26), 229-231,
611 doi:10.1002/2013EO260002.

612 Munekane, H. (2013), Coseismic and early postseismic slips associated with the 2011 off the
613 Pacific coast of Tohoku Earthquake sequence: EOF analysis of GPS kinematic time series, *Earth*
614 *Planet Sp*, *64*(12), 3, doi:10.5047/eps.2012.07.009.

615 Nocquet, J.-M., P. Jarrin, M. Vallée, P. Mothes, R. Grandin, F. Rolandone, B. Delouis, H. Yepes,
616 Y. Font, and D. Fuentes (2016), Supercycle at the Ecuadorian subduction zone revealed after
617 the 2016 Pedernales earthquake, *Nature Geoscience*, *10*(2), 145-149. doi: 10.1038/ngeo2864.

618 Nocquet, J.-M., J. Villegas-Lanza, M. Chlieh, P. Mothes, F. Rolandone, P. Jarrin, D. Cisneros, A.
619 Alvarado, L. Audin, and F. Bondoux (2014), Motion of continental slivers and creeping
620 subduction in the northern Andes, *Nature Geoscience*, *7*(4), 287-291. doi: 10.1038/ngeo2099.

621 Noda, H., and N. Lapusta (2013), Stable creeping fault segments can become destructive as a
622 result of dynamic weakening, *Nature*, *493*(7433), 518-521. doi: 10.1038/nature11703.

623 Okada, Y. (1992), Internal deformation due to shear and tensile faults in a half-space, *Bulletin of*
624 *the Seismological Society of America*, *82*(2), 1018-1040.

625 Ortega Culaciati, F. H. (2013), Aseismic deformation in subduction megathrusts: Central Andes
626 and North-East Japan, 198 pp, California Institute of Technology, PhD thesis.

627 Perfettini, H., and J. P. Ampuero (2008), Dynamics of a velocity strengthening fault region:
628 Implications for slow earthquakes and postseismic slip, *Journal of Geophysical Research: Solid*
629 *Earth*, *113*(B9). doi: 10.1029/2007JB005398.

630 Perfettini, H., J.-P. Avouac, H. Tavera, A. Kositsky, J.-M. Nocquet, F. Bondoux, M. Chlieh, A.
631 Sladen, L. Audin, and D. L. Farber (2010), Seismic and aseismic slip on the Central Peru
632 megathrust, *Nature*, *465*(7294), 78-81. doi: 10.1038/nature09062.

633 Perfettini, H., and J. P. Avouac (2004), Postseismic relaxation driven by brittle creep: A possible
634 mechanism to reconcile geodetic measurements and the decay rate of aftershocks, application
635 to the Chi-Chi earthquake, Taiwan, *Journal of Geophysical Research: Solid Earth*, *109*(B2), B02304,
636 doi:10.1029/2003JB002488.

637 Rolandone, F., J.-M. Nocquet, P. Mothes, P. Jarrin, M. Vallée, N. Cubas, S. Hernandez, M. Plain,
638 S. Vaca, and Y. Font (2018), Areas prone to slow slip events impede earthquake rupture
639 propagation and promote afterslip, *Science Advances*, *4*, eaao6596. doi: 10.1126/sciadv.aao6596.

640 Salman, R., E. M. Hill, L. Feng, E. O. Lindsey, D. M. Veedu, S. Barbot, P. Banerjee, I. Hermawan,
641 and D. H. Natawidjaja (2018), Piecemeal rupture of the Mentawai patch, Sumatra: The 2008 M_w
642 7.2 North Pagai earthquake sequence, *Journal of Geophysical Research: Solid Earth*. doi:
643 10.1002/2017JB014341.

644 Segovia, M., Y. Font, M. Régnier, P. Charvis, A. Galve, J.-M. Nocquet, P. Jarrín, Y. Hello, M. Ruiz,
645 and A. Pazmiño (2018), Seismicity distribution near a subducting seamount in the central
646 Ecuadorian subduction zone, space-time relation to a slow-slip event, *Tectonics*, *37*(7), 2106-
647 2123, doi:10.1029/2017TC004771.

648 Sennson, J. L., and S. L. Beck (1996), Historical 1942 Ecuador and 1942 Peru subduction
649 earthquakes and earthquake cycles along Colombia-Ecuador and Peru subduction segments,
650 *pure and applied geophysics*, *146*(1), 67-101, doi:10.1007/bf00876670.

651 Sladen, A., H. Tavera, M. Simons, J. P. Avouac, A. O. Konca, H. Perfettini, L. Audin, E. J. Fielding,
652 F. Ortega, and R. Cavagnoud (2010), Source model of the 2007 M_w 8.0 Pisco, Peru earthquake:
653 Implications for seismogenic behavior of subduction megathrusts, *Journal of Geophysical Research:*
654 *Solid Earth*, *115*(B2), doi:10.1029/2009JB006429.

655 Stein, R. S. (1999), The role of stress transfer in earthquake occurrence, *Nature*, *402*, 605-609.
656 doi: 10.1038/45144.

657 Tsang, L. L. H., E. M. Hill, S. Barbot, Q. Qiu, L. Feng, I. Hermawan, P. Banerjee, and D. H.
658 Natawidjaja (2016), Afterslip following the 2007 M_w 8.4 Bengkulu earthquake in Sumatra loaded
659 the 2010 M_w 7.8 Mentawai tsunami earthquake rupture zone, *Journal of Geophysical Research:*
660 *Solid Earth*, *121*(12), 9034-9049, doi:10.1002/2016JB013432.

661 Tung, S., and T. Masterlark (2018), Delayed Poroelastic Triggering of the 2016 October Visso
662 Earthquake by the August Amatrice Earthquake, Italy, *Geophysical Research Letters*, *45*(5), 2221-
663 2229, doi:10.1002/2017GL076453.

664 Twardzik, C., M. Vergnolle, A. Sladen, and A. Avallone (2019), Unravelling the contribution of
665 early postseismic deformation using sub-daily GNSS positioning, *Scientific Reports*.

666 Vaca, S., M. Vallée, J.-M. Nocquet, J. Battaglia, and M. Régnier (2018), Recurrent slow slip events
667 as a barrier to the northward rupture propagation of the 2016 Pedernales earthquake (Central
668 Ecuador), *Tectonophysics*, *724-725*, 80-92, doi:10.1016/j.tecto.2017.12.012.

669 Vallée, M., et al. (2013), Intense interface seismicity triggered by a shallow slow slip event in the
670 Central Ecuador subduction zone, *Journal of Geophysical Research: Solid Earth*, *118*(6), 2965-2981,
671 doi:10.1002/jgrb.50216.

672 Yabe, S., and S. Ide (2018), Why do aftershocks occur within the rupture area of a large
673 earthquake?, *Geophysical Research Letters*, *45*(10), 4780-4787, doi:10.1029/2018GL077843.

674 Ye, L., H. Kanamori, J.-P. Avouac, L. Li, K. F. Cheung, and T. Lay (2016), The 16 April 2016,
675 M_W7.8 (M_S7.5) Ecuador earthquake: A quasi-repeat of the 1942 M_S7.5 earthquake and partial re-
676 rupture of the 1906 M_S8.6 Colombia–Ecuador earthquake, *Earth and Planetary Science Letters*,
677 *454*, 248-258, doi:10.1016/j.epsl.2016.09.006.
678

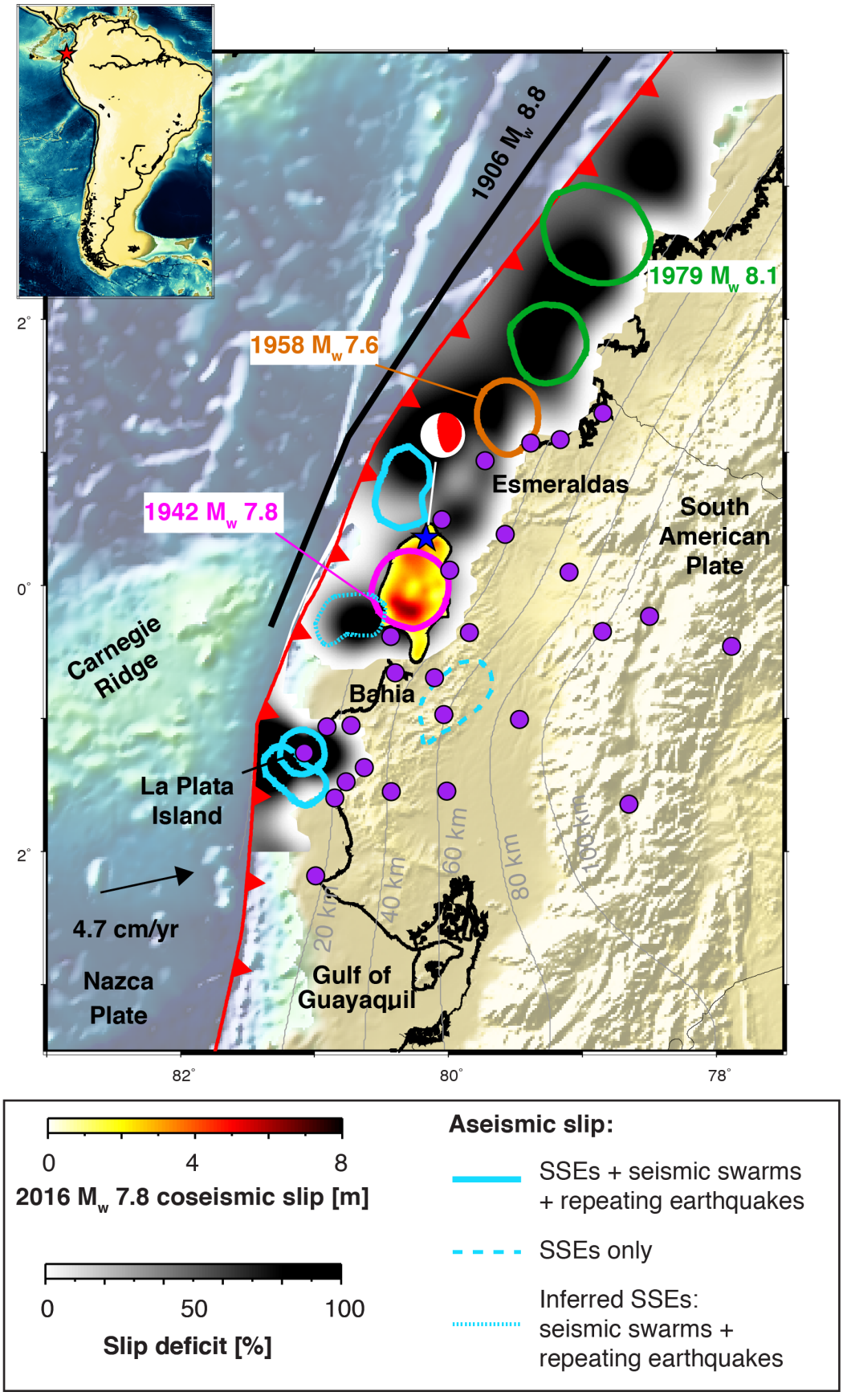
1906 M$_w$ 8.8
1979 M$_w$ 8.1
1958 M$_w$ 7.6
1942 M$_w$ 7.8
Esmeraldas
South American Plate
Carnegie Ridge
Bahia
La Plata Island
4.7 cm/yr
Nazca Plate
Gulf of Guayaquil
20 km
40 km
60 km
80 km
100 km
2°
0°
2°
82°
80°
78°
0
4
8
2016 M$_w$ 7.8 coseismic slip [m]
0
50
100
Slip deficit [%]
Aseismic slip:
SSEs + seismic swarms + repeating earthquakes
SSEs only
Inferred SSEs: seismic swarms + repeating earthquakes

679

Figure 1. (a) Interseismic slip deficit, seismic and aseismic events along the Ecuadorian megathrust. Coloured distribution of the 2016 Pedernales earthquake coseismic slip is from Nocquet et al. [2016]. Grayscale distribution of interseismic slip deficit (saturated at 80 %) is from Nocquet et al. [2016] and Collot et al. [2017]. Blue star: epicentre location of the 2016 M_w 7.8 Pedernales earthquake. Regions with coloured outline: High-slip areas of the 1942 (pink), 1958 (orange-brown) and 1979 (green) rupture zones [Beck and Ruff, 1984; Swenson and Beck, 1996; compiled by Chlieh et al., 2014]. Outlined in cyan: slow slip events, seismic swarms and repeating earthquakes reported and compiled by Rolandone et al. [2018]. Thick black line: rupture extent of the 1906 earthquake, from Kanamori and McNally [1984]. Grey lines and labels: Slab depth contours from Slab 1.0 [Hayes et al., 2012]. Purple circles: GPS stations used in this study. Inset: geographical setting and location of study indicated by the red star.

693 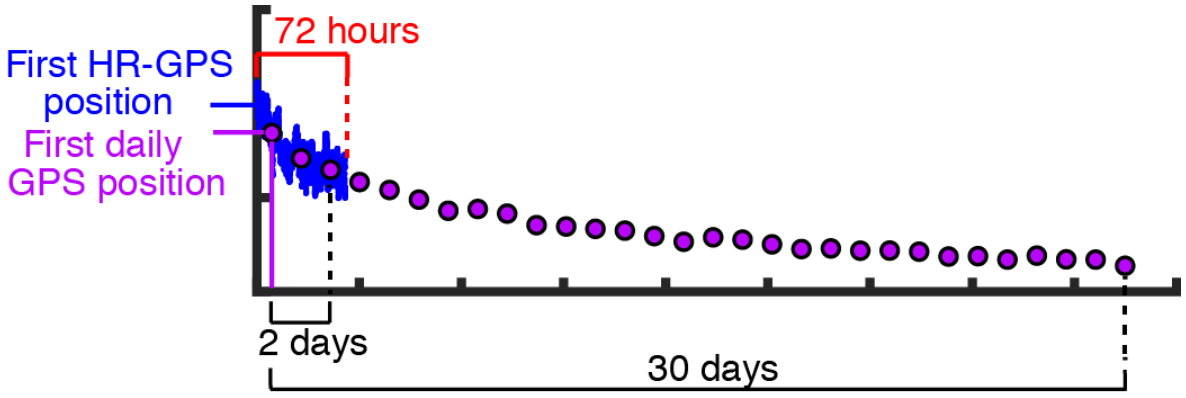

694 **Figure 2. Schematic of HR-GPS and daily GPS time series at one station**
695 **component, showing the three afterslip models that we estimated: (1) 72-hour**
696 **model with HR-GPS time series, (2) 2-day model with the first three daily GPS**
697 **positions, and (3) 30-day model with daily GPS time series spanning 30 days after**
698 **the earthquake.**

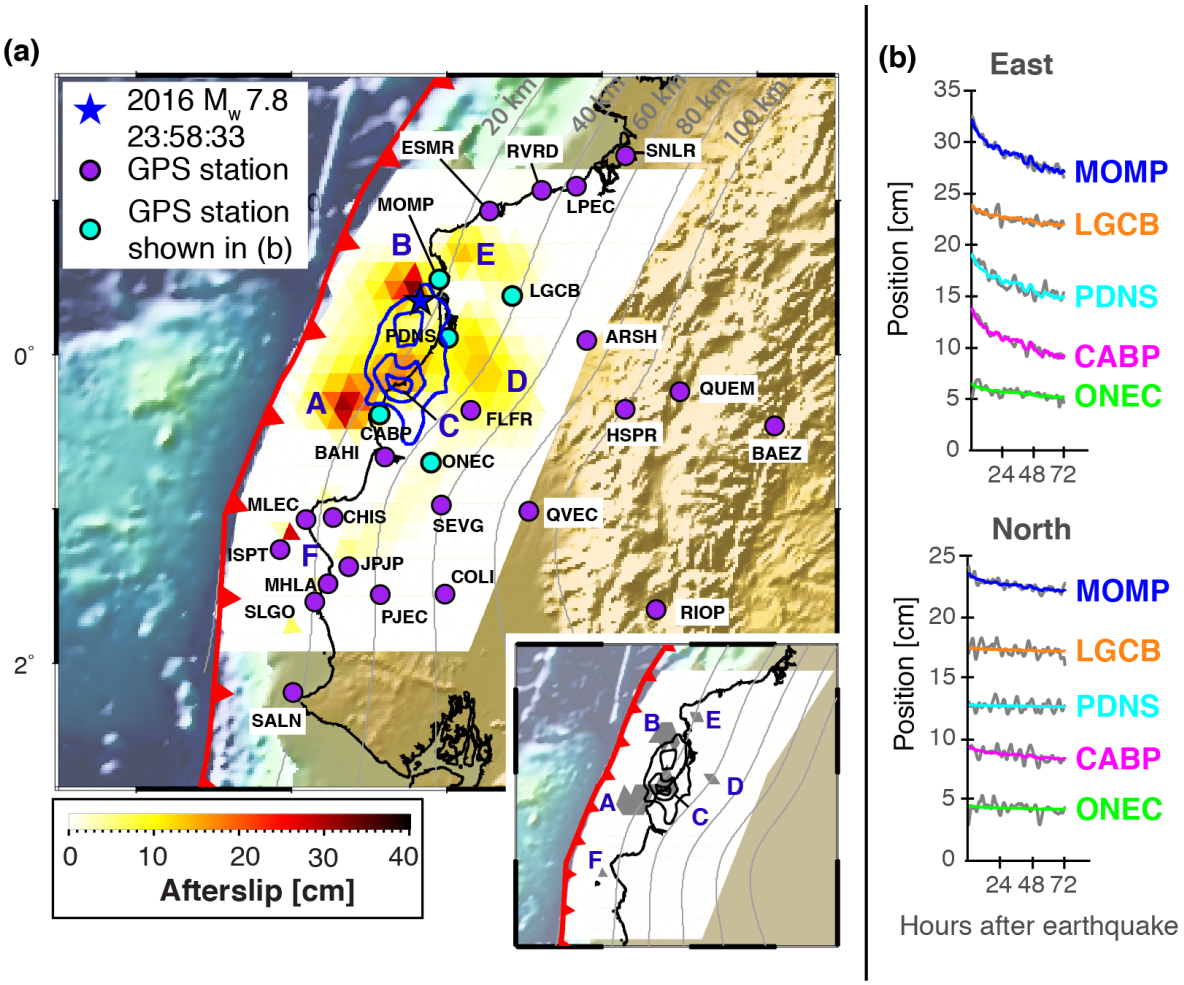

699

700 **Figure 3. (a) Reference model: Spatial distribution of cumulative afterslip in the**
701 **first 72 hours, obtained by inverting HR-GPS time series filtered with a cut-off**
702 **period of ~2.7 hours. Inset: areas of > 10 cm of cumulative afterslip common to all**
703 **five inversion models (using time series with various degrees of filtering applied,**
704 **see Figure S9). Blue contours: 1, 3 and 5 m coseismic slip contours from Nocquet**
705 **et al. [2016]. See Figure 1 for details of slab depth contours. Areas A to F are**
706 **discussed in the text. (b) Data (grey) and model (colours) time series at**
707 **representative GPS stations (highlighted in cyan in (a)). See Figure S10 for the**
708 **data-model fits at all stations.**

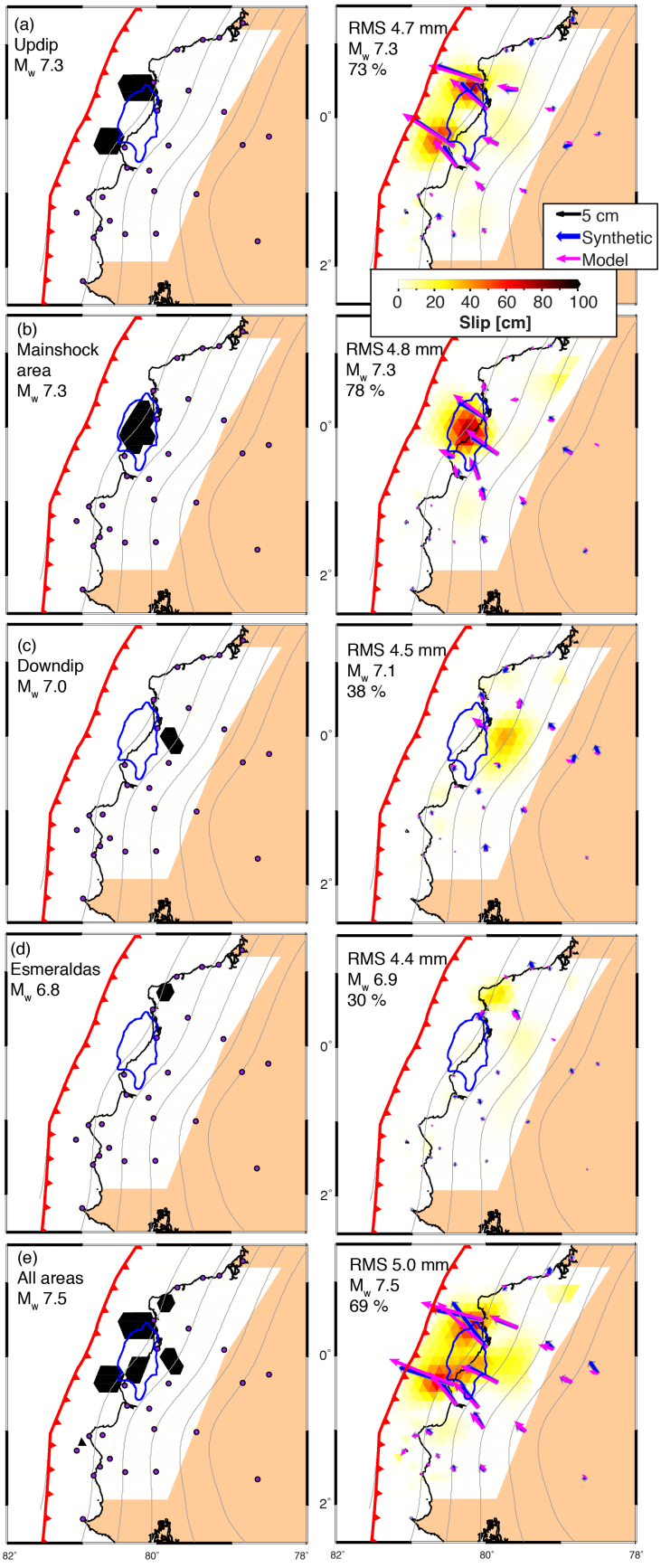
(a)
Updip
M_w 7.3
RMS 4.7 mm
M_w 7.3
73 %
5 cm
Synthetic
Model
0 20 40 60 80 100
Slip [cm]
(b)
Mainshock
area
M_w 7.3
RMS 4.8 mm
M_w 7.3
78 %
(c)
Downdip
M_w 7.0
RMS 4.5 mm
M_w 7.1
38 %
(d)
Esmeraldas
M_w 6.8
RMS 4.4 mm
M_w 6.9
30 %
(e)
All areas
M_w 7.5
RMS 5.0 mm
M_w 7.5
69 %
0°
2°
82°
80°
78°

709

Figure 4. Synthetic tests showing slip recovery in various areas. (a)-(e): Left: input synthetic slip distribution. M_w of each synthetic slip distribution is shown in the upper left corner. Right: recovered slip distribution estimated by inverting model time series of the synthetic slip distribution. Root mean square (RMS) of data-model fits, M_w of the recovered slip model and percentage of slip recovered are shown in the upper left corner. See Figure 3 for details of other contours.

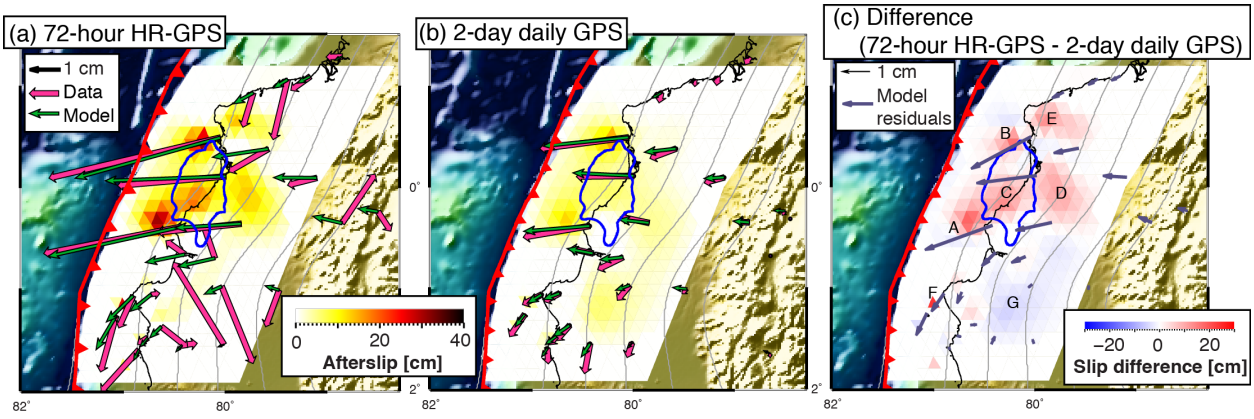

Figure 5. Cumulative afterslip models estimated with (a) 72-hour HR-GPS time series (reference model shown in Figure 3), (b) time series spanning the first 3 daily GPS positions after the day of the earthquake, and (c) difference between models (a) and (b). Data and model vector of cumulative displacements in (a) are obtained by differencing the mean average position in a 1-hour window at the beginning and end of the time series, whereas those in (b) are calculated by differencing the first and last points in the time series. Model residual vectors in (c) are calculated by subtracting the cumulative model displacements in (b) from those in (a). See Figure 3 for details of other contours.

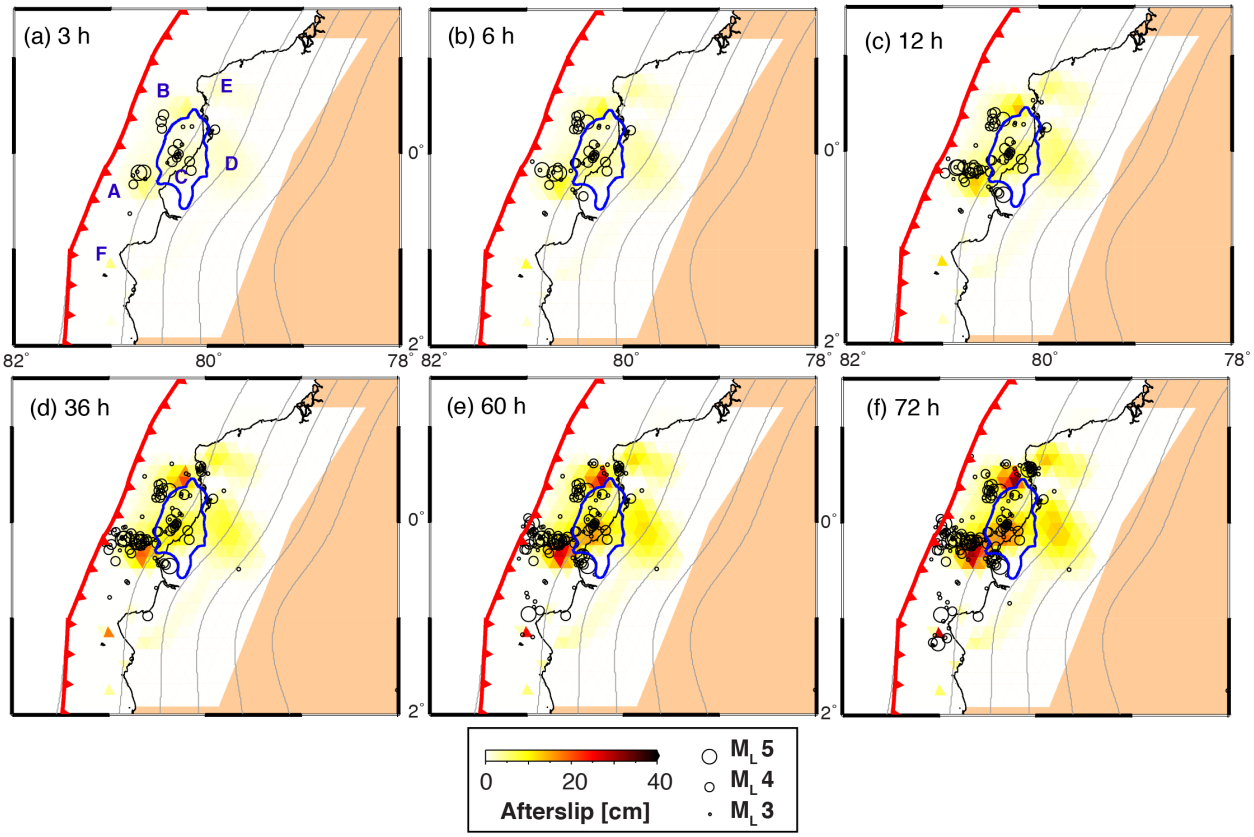

726

727 **Figure 6. (a)-(f): Spatio-temporal evolution of cumulative afterslip in the first 72**

728 **hours, and of M_L>3.5 relocated aftershocks from Agurto-Detzel et al. (submitted)**

729 **(sized by magnitude). Time in hours is indicated in the upper left corner. See**

730 **Figure 3 for details of other contours.**

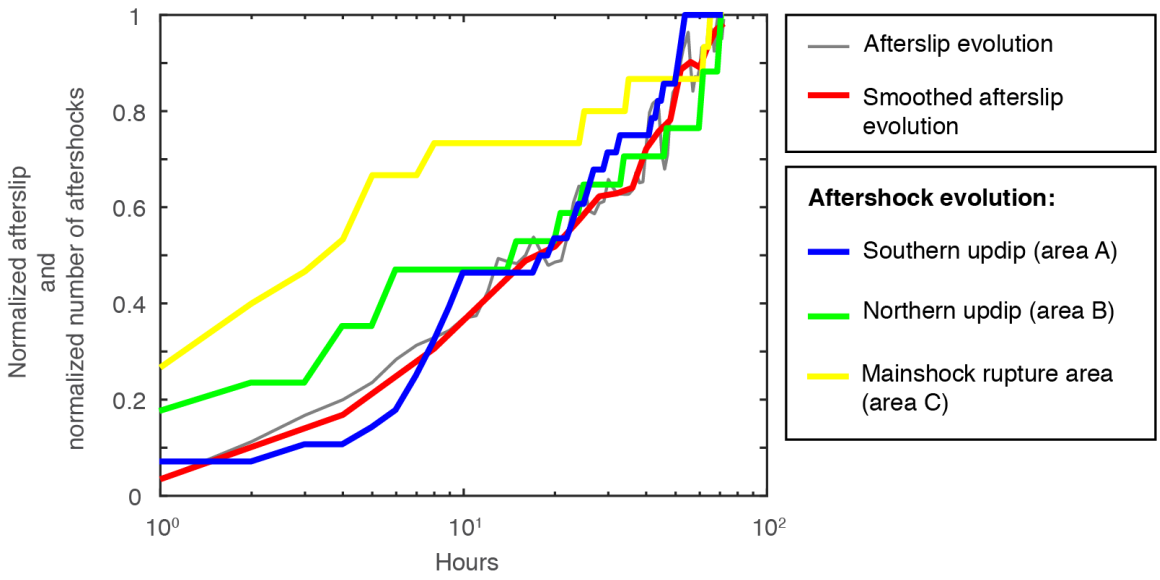

731

732 **Figure 7. Temporal evolution of afterslip and relocated aftershocks in three main**

733 **afterslip areas. The smoothed afterslip curve (red) is obtained by estimating the**

734 **mean cumulative afterslip in an 8-hour window, with a sliding window of 4 hours.**

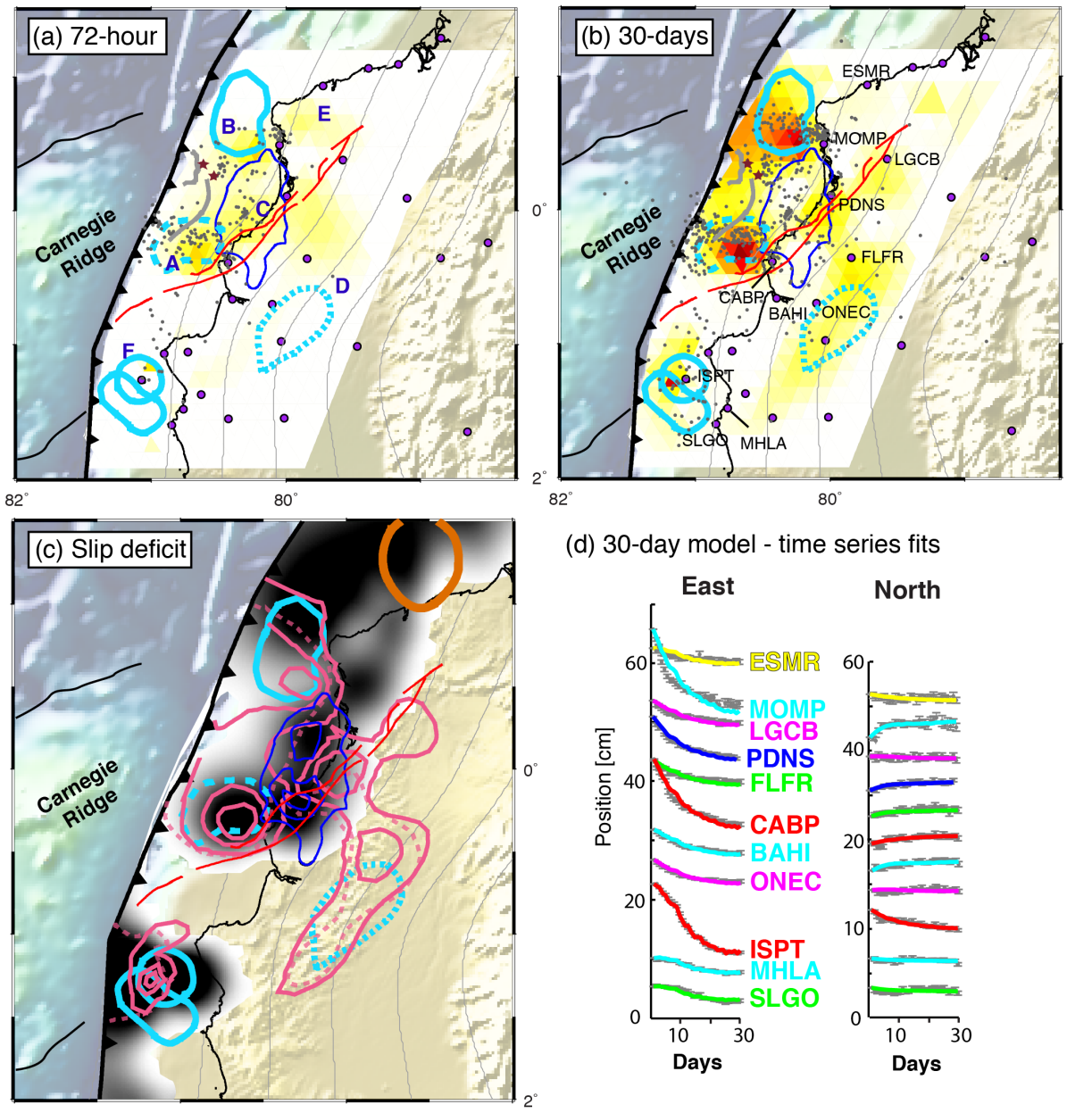
(a) 72-hour
(b) 30-days
(c) Slip deficit
(d) 30-day model - time series fits
Carnegie Ridge
A
B
C
D
E
F
ESMR
MOMP
LGCB
PDNS
FLFR
CABP
BAHI
ONEC
ISPT
MHLA
SLGO
82°
80°
0°
2°
East
North
Position [cm]
Days
Legend
Afterslip [cm]
Slip deficit [%]
1, 3 and 5 m coseismic slip contour [Nocquet et al., 2016]
10 cm afterslip contour [Rolandone et al., 2018]
10, 30, 50 cm afterslip contour of 30-day model from this study
SSEs + seismic swarms + repeating earthquakes
SSEs only
Inferred SSEs: seismic swarms + repeating earthquakes
High slip area of the 1958 earthquake
Jama fault zone
Subducted seamount peaks (stars) and fracture fronts (grey) associated with seamount subduction [Marcaillou et al., 2016]
GPS station
$M_L \geq 3.5$ aftershocks from Agurto-Detzel et al. (submitted)

735

736 **Figure 8. (a) 72-hour, and (b) 30-day afterslip models, plotted with the same scale.**
737 **(c) Spatial relationship between patterns of interseismic slip deficit (grayscale slip**
738 **distribution, saturated at 80 %) and various slip areas. See Figures 1 and 3 for**
739 **details of other contours and studies from which the slip deficit maps, slow slip**
740 **events and earthquake rupture areas were obtained. Areas A to F are discussed in**
741 **the text. (d) Time series of data-model fits at representative stations labeled in (b).**

742

Afterslip area	Model resolution indicator	Geodetic moment, Mo [N m]						$\frac{Mo_{72hour}}{Mo_{2days}}$	$\frac{Mo_{72hour}}{Mo_{30days}} \times 100$ (%)	$\frac{Mo_{2days}}{Mo_{30days}} \times 100$ (%)
		2-day (daily GPS)	2-day Mo/km²	72-hour (HR-GPS)	72-hour Mo/km²	30-day (daily GPS)	30-day Mo/km²			
A	Well resolved	4.78E+18	1.59E+09	9.25E+18	3.07E+09	2.82E+19	9.33E+09	1.94	33	17
B	Well resolved	5.62E+18	1.84E+09	8.28E+18	2.71E+09	3.14E+19	1.03E+10	1.47	26	18
C	Well resolved	4.44E+18	1.37E+09	1.02E+19	3.15E+09	9.69E+18	2.99E+09	2.29	105	46
D	Less well resolved	4.47E+18	8.77E+08	1.02E+19	2.00E+09	2.18E+19	4.27E+09	2.28	47	21
E	Less well resolved	3.93E+16	6.85E+07	1.67E+18	2.91E+09	7.05E+17	1.23E+09	42.5	237	6
F	Poorly resolved	3.45E+17	8.59E+07	8.86E+17	2.21E+08	1.03E+19	2.58E+09	2.57	9	3
Total	-	3.23E+19 (M_w 6.97)	-	5.22E+19 (M_w 7.11)	-	1.81E+20 (M_w 7.47)	-	1.62	29	18

743

744 **Table 1. Estimated geodetic moment in peak afterslip areas for each model.**

745 **Calculations are based on a constant rigidity of 30 GPa.**